Quantum Electronics **51** (8) 655–669 (2021)

REVIEW

https://doi.org/10.1070/QEL17566

Modern methods of detecting single photons and their application in quantum communications

A.A. Koziy, A.V. Losev, V.V. Zavodilenko, Yu.V. Kurochkin, A.A. Gorbatsevich

Abstract. **We consider main methods for detecting single photons used in quantum communications, including the quantum key distribution (QKD) technology. Two most promising single photon detectors (SPDs) based on superconducting nanowires and on a single-photon avalanche diode are described. The most effective SPD designs are presented and their advantages and disadvantages are analysed from the point of view of the possibility of their use in QKD devices. The results of the work of various scientific groups conducting research on QKD are discussed, which makes it possible to trace the trends in the global technological development of this industry over the past five years.**

Keywords: *single photon detector, quantum key distribution, superconducting nanowires, single-photon avalanche diode.*

1. Introduction

Cryptography is the science about methods for ensuring confidentiality (impossibility of reading information by eavsdroppers), data integrity (impossibility of imperceptible change of information), authentication (verification of authorship or other properties of an object), and encryption (data encoding) [1]. In classical cryptography, communication between two users is secured by using symmetric encryption (the simplest example is a one-time pad [2]) and asymmetric encryption protocols (RSA algorithm [3, 4], Diffie–Hellman protocol [5, 6]). The security of these cryptosystems is based on certain mathematical transformations that can be performed on a message by two legitimate users (Alice and Bob). However, as a result of the creation of a sufficiently powerful quantum computer, some widely used cryptosystems (RSA, Diffie–Hellman and other systems based on factorisation of composite numbers) will be cracked in a matter of seconds, and other cryptographic protocols will significantly become less secure.

In 2019, Google made an attempt to demonstrate 'quantum supremacy': their prototype of a superconducting quantum computer was able to solve the factorisation problem much faster than a classical computer [7]. In December 2020, a report was published on the achievements of Chinese scientists in the field of computing on a photonic quantum computer – their prototype was named Jiuzhang, and in terms of the declared speed it surpassed the Google quantum computer by 10 billion times [8]. The main problem of loss of security of cryptosystems is associated with the existence of Shor's [9] and Grover's [10] algorithms implemented on a quantum computer. Moreover, in this area, new quantum algorithms, machine learning algorithms are being actively developed, which can lead to an even greater loss of security of existing cryptographic systems [11].

The security of quantum cryptography is due to the physical uncertainty that arises when measuring a quantum object (photon). In 1984, Bennett and Brassard [12] proposed the first quantum communication protocol BB84 [quantum key distribution (QKD)], with the help of which it became possible to implement much more secure symmetric cryptography systems that are immune to potential attacks on both quantum and classic computers. In this protocol, single photons polarised in two non-orthogonal bases were transmitted over an open communication line. In 1992, this protocol was modified – its creators added 'decoy states', which made it possible to defend against a split-photon attack and significantly increased the security of this system [13]. There is also a polarisation encoding method, which is used to organise quantum channels through open space, and currently communication with orbiting satellites has been implemented [14]. In fibre-optic communication lines, phase encoding based on Mach–Zehnder interferometers is often used [15].

All existing systems of quantum cryptography carry out certain operations (transmission via fibre-optic channels, phase modulation, and polarisation change) on single quantum objects, i.e. photons. A nontrivial problem arises in the algorithm – the direct detection of a single photon. Moreover, for the efficient operation of a QKD system, certain requirements are imposed on a single photon detector (SPD), which include such parameters as the photon detection efficiency (PDE), dark count rate (DCR), maximum frequency detection, photon number resolution (PNR), weight and size characteristics, and cost. Depending on the problem that the QKD system must solve, certain parameters will dominate:

A.A. Koziy, Yu.V. Kurochkin QRate, ul. Novaya 100, Skolkovo, 143026 Odintsovo, Moscow region, Russia; Quantum Communications Centre of NTI, National University of Science and Technology MISiS, Leninsky prosp. 4, 119049 Moscow, Russia; e-mail: a.kozii@goqrate.com;
A.V. Losev QRate, ul. Novaya 100, Skolkovo, 143026 Odintsovo, Moscow region, Russia; Quantum Communications Centre of NTI, National University of Science and Technology MISiS, Leninsky prosp. 4, 119049 Moscow, Russia; National Research University of Electronic Technology (MIET), pl. Shokina 1, 124498 Zelenograd, Russia;
V.V. Zavodilenko QRate, ul. Novaya 100, Skolkovo, 143026 Odintsovo, Moscow region, Russia;
A.A. Gorbatsevich National Research University of Electronic Technology (MIET), pl. Shokina 1, 124498 Zelenograd, Russia; Lebedev Physical Institute, Russian Academy of Sciences, Leninsky prosp. 53, 119991 Moscow, Russia

Received 31 May 2021
Kvantovaya Elektronika **51** (8) 655–669 (2021)
Translated by I.A. Ulitkin

for example, to implement a compact QKD system (suitable for a standard server rack), the main parameters are the signal-to-noise ratio and weight and size characteristics; to transmit a key over long distances (more than 100 km), the parameters in question are the noise level and photon detection efficiency; and to achieve the maximum key generation rate, the maximum detection frequency is needed.

Currently, the most widely used SPDs are based on superconducting nanowires [superconducting nanowire single photon detectors (SNSPDs)] [16] and on single-photon avalanche diodes (SPADs) [17]. In order to draw a conclusion about the type of an SPD to be used in which applications (including for QKDs), in Sections 2 and 3 we analyse the physical processes occurring in SNSPDs and SPADs, respectively, and present their typical operating parameters. In Section 4, a conclusion is drawn about the optimal use of one or another SPDs for various applications.

2. SPDs based on superconducting nanowires

Before SNSPDs were invented and achieved high performance, single-photon radiation was detected by superconducting detectors, in which some element sensitive to single-photon radiation was cooled to sub-Kelvin temperatures: a superconducting tunnel junction (STJ) [18], a transition-edge sensor (TES) [19], and a kinetic inductance detector (KID) [20].

In 2001, Gol'tsman and coworkers [21] demonstrated a single-photon detector for a wavelength of 810 nm, the operating principle of which is based on current-biased superconducting niobium nitride (NbN) microbridges. In 2002, Verevkin et al. [22] proposed to use a meander structure instead of microbridges, and in 2003 this device found its first commercial application in the field of testing integrated circuits [23]. The demonstrated potential of such an SPD made an SNSPD the leader among superconducting single-photon detectors. The main advantages over competitors were the low level of the dark count rate and the high efficiency of photon detection [24–27].

The SNSPD is currently the most sensitive to single-photon radiation and is undergoing numerous design modifications to achieve the performance targets required for specific applications. The most common SNSPD structure for use in QKD is as follows: a rather thin (less than 10 nm thick) and narrow (approximately 100 nm wide) nanowire, coiled in a meander with an active region diameter of about 10 μm and a fill factor of ~0.5, is made on a silicon substrate with a grown dielectric mirror. The system is cooled to temperatures below the critical superconductivity temperature, $T < T_{crit}$, and a current I flows through the nanowire, which is less than the critical current I_{crit}, at which superconductivity is lost. At present, the detection mechanism is not yet fully understood, and two main models can be distinguished for which good agreement between theory and experiment is observed.

At high photon energies, the 'hotspot' diffusion model is usually used [28, 29]. When a photon is absorbed by a nanowire, Cooper pairs are destroyed, followed by the formation of thermally excited quasi-particles. This leads to a local increase in temperature in the absorption region – the creation of a hotspot. In contrast to the simpler hotspot model [21], the region of the spot in the model that takes into account diffusion does lose superconducting properties. By reducing the total number of Cooper pairs to maintain a constant current through the nanowire, the movement velocity of the remaining Cooper pairs increases. If their velocity exceeds a certain critical velocity v_{crit}, then they are destroyed, which, as a result, leads to the transition of the nanowire to the normal (nonsuperconducting) state.

At low photon energies, the vortex model is usually used [28, 29]. In this model, two mechanisms of the transition of a nanowire to the normal state are considered, i.e. due to a single magnetic vortex generated at the nanowire boundary, and due to a vortex–antivortex pair generated in the centre of the nanowire.

In the first case, due to absorption of a photon, a region of a nanowire with an increased temperature is formed; in this case, in this region, the threshold energy for the entry of the magnetic vortex into the nanowire decreases. Due to the flowing current, the resulting vortex envelops the nanowire, which leads to the destruction of its superconducting state. Likharev [30] showed that the effect of the entrance of a single vortex can be observed only for a nanowire of width $w > 4.4\xi_L$, where ξ_L is the coherence length of Cooper pairs (Likharev's criterion). The coherence length depends on the material in question: for Nb, NbN, NbTiN and WSi, ξ_L = 38, 6.5, 170 and 7 nm, respectively.

Let us consider the second scenario. When a photon is absorbed in a hotspot, a vortex–antivortex pair is formed. Under the action of the Lorentz force, the vortex and antivortex begin to move in opposite directions, crossing the nanowire. In the case of the destruction of the vortex–antivortex pair, there occurs a transition of the nanowire to the normal state.

With different internal SNSPD parameters (which cannot be changed for the assembled detector), such as nanowire material, thickness, width and shape, different photon detection mechanisms will dominate. Nevertheless, the processes caused by these mechanisms can occur simultaneously.

After the nanowire passes into the normal state, its resistance becomes equal to ~1 kΩ. A sharp change in resistance leads to the occurrence of transient processes with jumps in the output voltage, which is recorded by the control electronics. In addition, the nanowire begins to heat up. A quenching resistor with a nominal resistance $Z_0 = 10 - 100$ kΩ [31] is connected in parallel to the nanowire, which reduces the current flowing through the nanowire after the detector is triggered. In this case, two parallel relaxation processes take place: cooling of the nanowire with the recovery of superconducting properties and restoration of a given bias current. In fact, the recovery of superconductivity is much faster than the recovery of a given bias current. This is due to the fact that the nanowire rolled into a meander has a large kinetic inductance L, and the recovery time can be approximately estimated as $\tau = L/Z_0$. The bias current recovery time limits the maximum SNSPD detection frequency, since during this 'dead' time the detector is insensitive to incident radiation [24]. For an SNSPD, the characteristic dead time is $\tau \approx 10 - 100$ ns, which makes it possible to achieve a maximum response frequency of the detector, $\nu_{max} \approx 10 - 100$ MHz (see Table 1).

In SNSPDs with passive quenching and recovery, there is a negative effect called 'latching', that is, the detector nanowire does not pass into a superconducting state, but remains in a resistive state [24]; in this case, the detector cannot register radiation. Positive feedback is observed for this effect, and it does not disappear by itself. One of the reasons for its occurrence is that the current through the nanowire is recovered before it becomes superconducting again. This problem often arises when the kinetic inductance of the nanowire is low (for

example, it is created not in the form of a meander structure, but in the form of a microbridge). In this case, an additional inductance is connected in series with the nanowire to prevent the latching effect [32]. To remove the detector from the latching mode, it is necessary to forcibly lower the bias current. The latching effect is not a property of the nanowire, but is caused by an incorrectly selected current bias circuit [31]. In order to completely eliminate latching without the use of complex bias circuits, circuits with active quenching are used, that is, the bias current is constant, but it is turned off if the output voltage exceeds the comparator operation threshold. Thus, after detection, the current is completely zeroed and reappears when the nanowire temperature approaches the critical one and the nanowire passes into a superconducting state [33]. The main mechanisms of SNSPD operation are schematically shown in Fig. 1.

Let us consider other main operational parameters of SNSPDs, which are essential when they are used in a QKD system.

An important characteristic is the timing jitter δt. This parameter is determined by the distribution of the detection time delay relative to the photon incidence time. The total width at half maximum (FWHM) of the given distribution is usually taken as the δt value, and it determines the temporal resolution of the detector. The shape of the timing jitter distribution for SNSPDs can be approximated by a normal distribution, which is quite convenient when constructing a theoretical model of the detector. The timing jitter of the detector strongly depends on the initial current I_0 and the photon energy: the higher the photon energy and the higher the current I_0, the lower the jitter [35]. Currently, the record value of jitter can be considered 2.6 ± 0.2 and 4.3 ± 0.2 ps for photons of visible radiation and with a wavelength of 1550 nm, respectively [36].

The noise characteristics for SNSPDs are determined by the dark count rate (DCR), that is, the count rate of the detector in the absence of useful (intentionally supplied) excitation light. There are several reasons for the detector's dark response.

1. External illumination associated with thermal photons generated in the optical fibre, with external photons transmitted through the optical fibre, or even high-energy cosmic particles. To eliminate external illumination, two main approaches are used. The first one is additional cooling of the optical fibre in one of the stages of the cryochamber to temperatures much higher than the superconductivity temperature $T_{crit} \approx 40$ K (Fig. 2a) [37]. Thus cooling is necessary to exclude a sharp temperature drop in the optical fibre – from room temperature to liquid helium temperatures – and to increase the system resource. In addition, thermal photons generated in optical fibre are subjected to high absorption. This is used as follows: an optical fibre of a certain length is wound inside one of the stages of the cryochamber and cooled to a temperature of 40 K in order to increase the fraction of absorbed photons and reduce the likelihood of new photons being produced. Note that at low temperatures the produc-

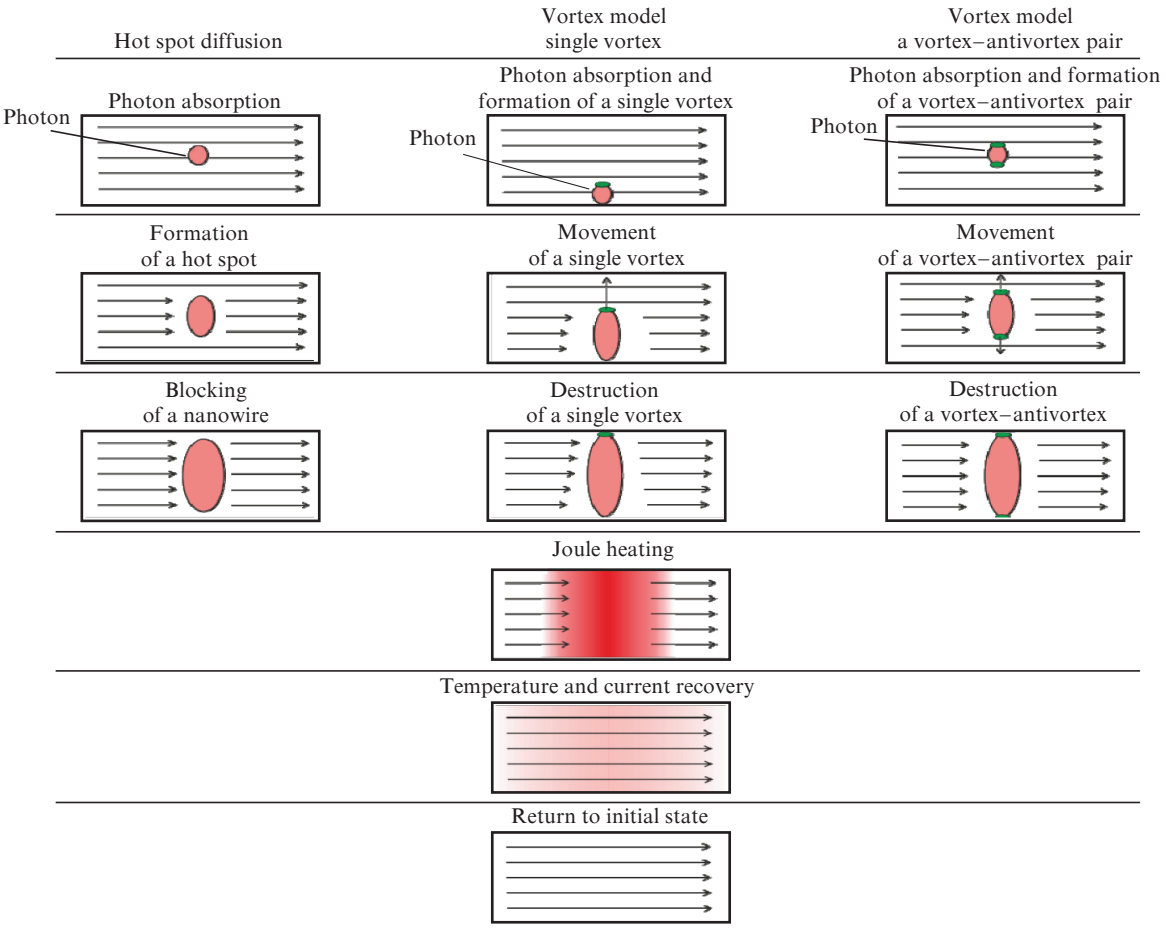

Figure 1. Basic mechanisms of SNSPD operation (schematic representation of the detection cycle [24, 34]).

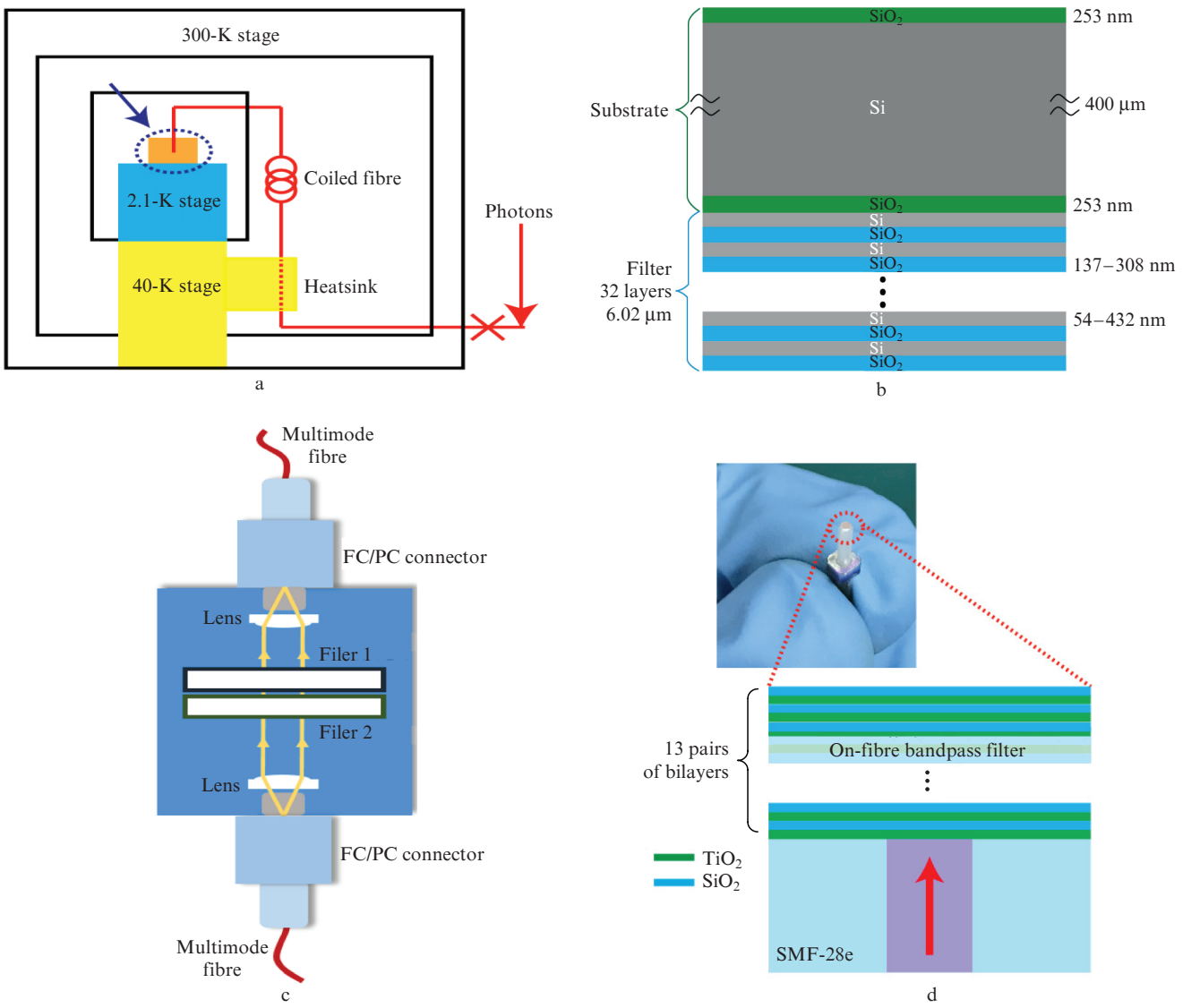

Figure 2. (Colour online) (a) Schematic of an SNSPD cryochamber [37], as well as (b–d) bandpass filters for on-chip SNSPDs with a wavelength of $\lambda = 1550$ nm (b) with superconducting nanowires [38], (c) in the form of separate cooled assemblies for multimode fibre [39] and (d) at the end of the fibre [37].

tion of long-wavelength photons is most likely, to which the detector is insensitive.

The second approach is to design bandpass filters – on a chip with superconducting nanowires, as separate cooled assemblies for multimode fibre, or at the end of optical fibre. Yang et al. [38] fabricated a filter on a chip, consisting of 32 layers of Si (thickness varied from 54 to 432 nm) and SiO_2 (thickness from 137 to 308 nm), deposited on the back side of the substrate (Fig. 2b). As a result, it was possible to obtain a filter bandpass of 1550 ± 25 nm with a transmittance of 88% and a total photon detection efficiency PDE ≈ 56% at DCR ≈ 1 Hz.

Zhang et al. [39] achieved a bandpass of 1550 ± 12.5 nm (with a transmission coefficient of about 80%) by using a combination of two filters cooled to 40 K (Fig. 2c). Filter 1 was a commercially available 1550-nm bandpass filter (#87822, Edmund), but its disadvantage is that at $\lambda > 2000$ nm it has a fairly good photon transmittance. Filter 2 was a customised low-pass filter [39] to eliminate the shortcomings of the first filter. As a result of using a system of two filters, it was possible to obtain PDE ≈ 51% at DCR ≈ 100 Hz and increase the signal-to-noise ratio by 160 times in comparison with a detector without a filtering module.

The authors of [37] designed a filter integrated on the fibre end-face (Fig. 2d), consisting of 13 layers of SiO_2 (thickness varied from 264 to 530 nm) and TiO_2 (176 nm thick), and a bandpass of 1560 ± 20 nm was achieved; in this case, the photon detection efficiency decreased by only 3% (from 83%), and the DCR value decreased by 13 dB (down to 0.5 Hz).

2. Noise of the electronics. An unstable current source can cause the current to oscillate. At a sufficiently high average bias value (for example, $I \approx 0.8\, I_{crit}$), short-term excess of the critical current will occur, which will lead to the loss of the superconducting state in the nanowire and false triggering. Oscillations of the current can be generated by pulse voltage converters or external electromagnetic interference. In order to get rid of electronic noise, it is necessary to use better quality power supplies, add additional filters to the electrical circuit, and isolate the detector from potential sources of interference [40].

3. Internal noise. It is caused by mechanisms similar to the mechanisms for detecting low-energy photons – due to the for-

mation of single magnetic vortices or a vortex–antivortex pair. Unlike an absorbed photon, which causes a rather strong local heating of the nanowire, thermal fluctuations have much lower energies. Nevertheless, this leads to a decrease in the potential barrier for the entry of a single vortex, due to which it can tunnel into the nanowire. The energy of the potential barrier for the vortex–antivortex pair also decreases in a similar way. Internal noise is the limiting part of the DCR, since it is impossible to completely eliminate thermal fluctuations, in contrast to the noise of electronics and external illumination [29]. Thus, by significantly minimising the contributions of the two indicated parts of the DCR, it was possible to achieve a dark count rate DCR $\approx 10^{-4}$ Hz [41].

Photon detection efficiency (PDE) is defined as the probability that a single photon arriving at the detector will be detected. In this case, it is necessary to distinguish between internal (η_{dde}) and general (η_{sde}) detection efficiencies. To clarify the differences between these parameters, we introduce the following probabilities of events: η_{coupl} determines the probability of a photon to hit the sensitive area of the detector (possible obstacles are reflection and scattering in the region of the fibre-optic coupling and the sensitive region of the SNSPD); η_{abs} determines the probability of absorption of a photon by the nanowire material; and η_{reg} is the probability that, in the case of absorption of a photon, a stable hotspot is formed and the response is registered by the control electronics. Thus, η_{dde} and η_{sde} can be defined as [24]

$$\begin{cases} \eta_{\text{dde}} = \eta_{\text{abs}}\eta_{\text{reg}}, \\ \eta_{\text{sde}} = \eta_{\text{coupl}}\eta_{\text{abs}}\eta_{\text{reg}}. \end{cases} \quad (1)$$

In SNSPDs, there are no correlations between detector triggers at an arbitrary point in time and previous triggers, i.e., the detector does not exhibit an afterpulse effect. This property is a significant advantage of SNSPDs over semiconductor detectors in which this effect is present: first, the dark count in superconducting detectors does not depend on the intensity of the incident radiation; and, second, the detection processes can be considered as Markov processes, which greatly simplifies the processing of experimental data [42]. However, for example, Burenkov et al. [43] showed that under certain conditions, the SNSPD still has an afterpulse effect, which is not related to the physical processes occurring in the nanowire itself, but is generated by the processes of re-reflection of the output signal in the RF path of amplifiers. Thus, the afterpulse effect in SNSPDs can be observed, but it is a consequence of poor-quality control electronics and is not caused by physical processes occurring in the detecting element itself.

Figure 3 shows the schemes of the currently most promising SNSPD designs, that is, single-pixel and multi-pixel devices produced using single-layer or multilayer nanowires.

The classical topology of a nanowire on a substrate is a meander (Fig. 3a). A significant drawback of a meander structure is the detector's sensitivity to photon polarisation. Due to the geometric parameters of the meander (the typical nanowire width is 80 nm, the meander period is 160 nm, and the filling density is about 50% for 1550 nm [44]), it can be considered as a diffraction grating. Thus, for example, for horizontally polarised photons, the probability of being reflected from such a structure is greater than for vertically polarised photons. Some detectors are designed in such a way as to maximise the polarisation sensitivity [46]; however, this dependence is undesirable for use in QKD. To rule out this effect, fractal topologies are being developed (Fig. 3c) [45, 47], but such detectors are still laboratory samples.

QKD systems can make use of both single-pixel and multi-pixel (Fig. 3b) SNSPDs. Single-pixel devices have significantly lower noise levels (less than 1 Hz [37]). However, their maximum response rate is several times lower than that of multi-pixel detectors. This is due to the fact that rather complex control electronics allows one to control some pixels independently of others. Thus, if the limiting count rates for single-pixel detectors are about 100 MHz, then for multi-pixel detectors they can exceed 1 GHz. Zhang et al. [48] demonstrated a 16-pixel SNSPD, which has a limiting counting rate of 1.5 GHz.

The advantage of two-layer SNSPDs (see Fig. 3a) over single-layer ones is the increased photon absorption probability η_{abs}. Thus, for the NbN material, the optimal nanowire thickness is about 6–7 nm (see Table 1). At this thickness the probability of its registration η_{reg} is maximal in the case of photon absorption. However, the photon absorption probability η_{abs} significantly differs from unity (~0.9) even with the use of a system of optical resonators and mirrors. Double-layer nanowires make it possible to achieve a close-to-unity photon absorption probability, while the detection efficiency remains at the same level. The main difficulty in the fabrication of a two-layer structure is the making of two nanowires with identical properties. Moreover, an attempt was made to design an SNSPD with a three-layer nanowire structure; however, due to the described problem, the characteristics of such a detector were much worse than those of two-layer structures [44].

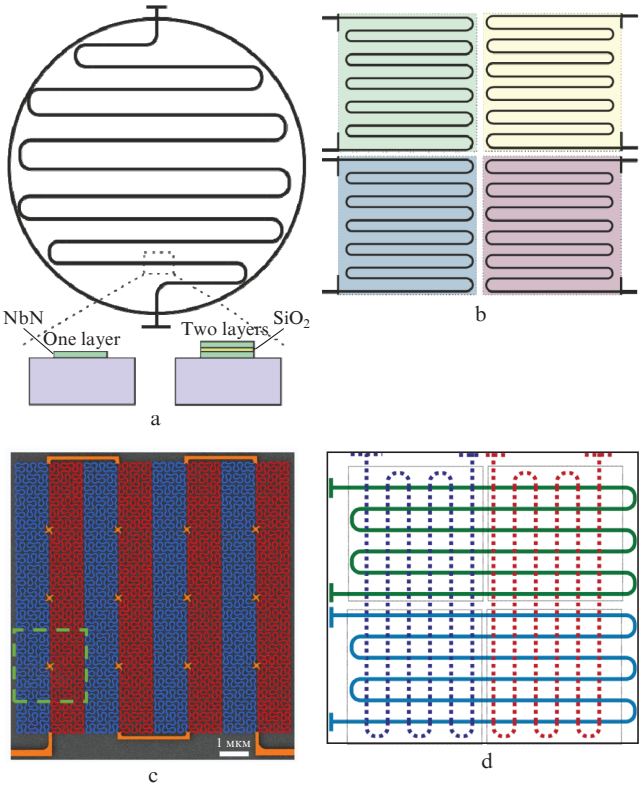

Figure 3. Schematic of SNSPD structures: (a) single-pixel meander structure, which can be made with both single-layer and double-layer nanowires; (b) multi-pixel meander structure; (c) single-pixel structure of fractal type [45]; and (d) multi-pixel structure using two-layer nanowires.

The operation principle of a multi-pixel detector with a two-layer nanowire (Fig. 3d) made it possible to significantly simplify the control electronics for such SNSPDs. In this system, the upper and lower layers consist of N meanders, which can be located both parallel and perpendicular to each other. The control is carried out for $2N$ square waves, instead of N^2 as it would be in single-layer SNSPD architecture. As a result, even for a system with 3×3 pixels, there is a gain in the simplicity of detector control. When a photon is absorbed, for example, by one of the upper nanowires, one of the lower nanowires is closed. Thus, in the case of their perpendicular arrangement, it is possible to accurately determine the position of the photon. The disadvantage of this system relative to single-layer multipixel SNSPDs is the significantly lower maximum response rate, which is proportional to N rather than N^2. Thus, for a 16-pixel detector with a similar architecture, it is possible to obtain a maximum count rate of about 400 MHz [49].

Numerous schemes have been developed to increase the photon absorption probability η_{abs}. Some of them with the best photon absorption parameters are shown in Fig. 4: a dielectric optical resonator [50, 51], a dielectric (or metal) mirror [52, 44], and 3D and 2D optical microcavities [53, 54].

In the case of a structure with an optical resonator, the nanowire is grown on a SiO_2 material and coated with a SiO layer on top. A pair of materials SiO_2/SiO makes it possible to confine a photon in a nanowire for a rather long time and significantly increase its average path length in it [50, 51].

A dielectric mirror for photons with $\lambda = 1550$ nm is usually produced by layer-by-layer deposition of SiO_2/Ta_2O_5 materials. The authors of Refs [44, 52] used a mirror consisting of 13 layers, the thickness of which was a quarter of the radiation wavelength. Thus, for photons with a wavelength of 850 nm, the thickness of SiO_2 is 145 nm, and for Ta_2O_5, 104 nm [52]. Using a mirror also increases the photon absorption probability η_{abs}.

You et al. [55] performed a theoretical comparison of these structures by means of numerical simulation. They showed that the photon absorption probability is higher in a structure with a dielectric mirror; however, such a structure is effective only for photons with a deviation of ±100 nm from the radiation wavelength determined by the structure design. If a sufficiently large wavelength spread (±250 nm) is possible for the received photons, the structure of the dielectric resonator turns out to be preferable.

The structure in Fig. 4c is an improved structure of the optical resonator shown in Fig. 4a. In this case, each line of the meander nanowire is placed in its own optical resonator made of hydrogen silsesquioxane (HSQ in the figure), the width of which is determined by the width of the nanowire itself. Due to the additional spatial limitation, photons experience multiple reflections not only in the vertical plane, as it happens in the structures in Figs 4a and 4b, but also in the horizontal plane. The main advantage of this structure is that it is possible to significantly reduce the meander filling factor without a drop in the photon absorption probability. This will result in a proportional decrease in kinetic inductance and DCR, in contrast to conventional SNSPD with a duty cycle of about 50%. Thus, Li et al. [53] presented the results of calculating such a structure for photons with $\lambda = 1550$ nm and

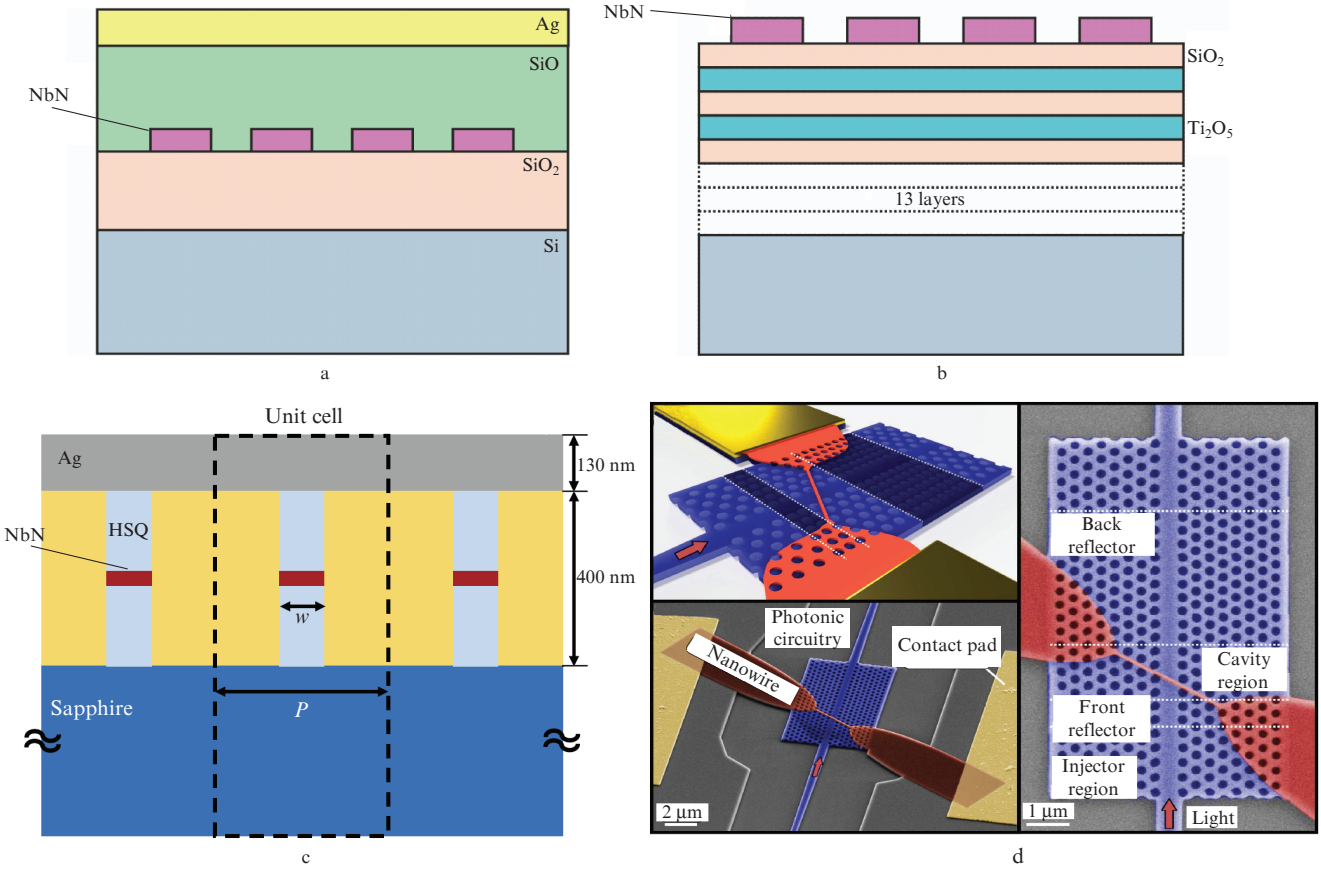

Figure 4. (Colour online) Structures designed to increase the photon absorption probability: (a) dielectric optical resonator [50, 51], (b) dielectric mirror [52, 44], (c) 3D optical microcavities [53], and (d) 2D optical microcavities [54].

showed that SNSPDs with such 3D microcavities have an optimal step parameter $P = 732$ nm, which corresponds to a filling factor of only 10.9%.

The structure shown in Fig. 4d is one of the examples of on-chip SNSPD implementation. In this case, there is no problem with the optimisation of the photon probability to hit the sensitive region η_{coupl}, since the optical radiation is supplied through the integrated waveguide. The main problem of such planar 2D structures is the low photon absorption probability η_{abs} relative to bulk structures. Munzberg et al. [54] managed to achieve a PDE > 60% by creating a complex geometry of a 2D microcavity consisting of a large number of holes, the size and location of which were optimised for a wavelength of ~1550 nm. This structure had a high spectral sensitivity with FWHM ≈ 5 nm, which is both an advantage and a disadvantage: The embedded active element filtering of photons with a wavelength different from the specified one makes it possible to almost completely eliminate the detection of light photons; however, the production of a structure with the required spectral characteristics is associated with high technological complexity (since it is necessary to observe high accuracy of producing a large number of elements with linear dimensions of the order of 100 nm). For example, in [54], the peak of the spectral sensitivity was at the wavelength $\lambda = 1542$ nm, while at $\lambda = 1550$ nm, the absorption efficiency was already about 10 times lower.

In 2017, Vodolazov [56] predicted that in an SNSPD scheme, the sensitive element can make use of microwires with a width of more than 1 μm rather than a nanowire with a width of ~100 nm. In this case, it is necessary to supply a bias current that is close enough to the current at which the Cooper pair is destroyed. In 2018, Korneeva et al. [25] succeeded in making a similar detector, in which a micrometer-wide bridge was used instead of a nanowire rolled into a meander. The detector with a micrometer-width sensitive element is called a superconducting microwave single photon detector (SMSPD). In 2019, Manova et al. [57] designed a detector with a photon detection efficiency of about 30%. In 2020, Chiles et al. [32] and independently of him Charaev et al. [58] succeeded in fabricating an SMSPD for photons with $\lambda = 1550$ nm and observing the PDE saturation effect with increasing bias current. In 2021, Xu et al. [59] reported on the making of an SMSPD with PDE ≈ 92.2% and DCR ≈ 200 Hz for $\lambda = 1550$ nm, which brought this type of detector closer in parameters to the best SNSPD specimens.

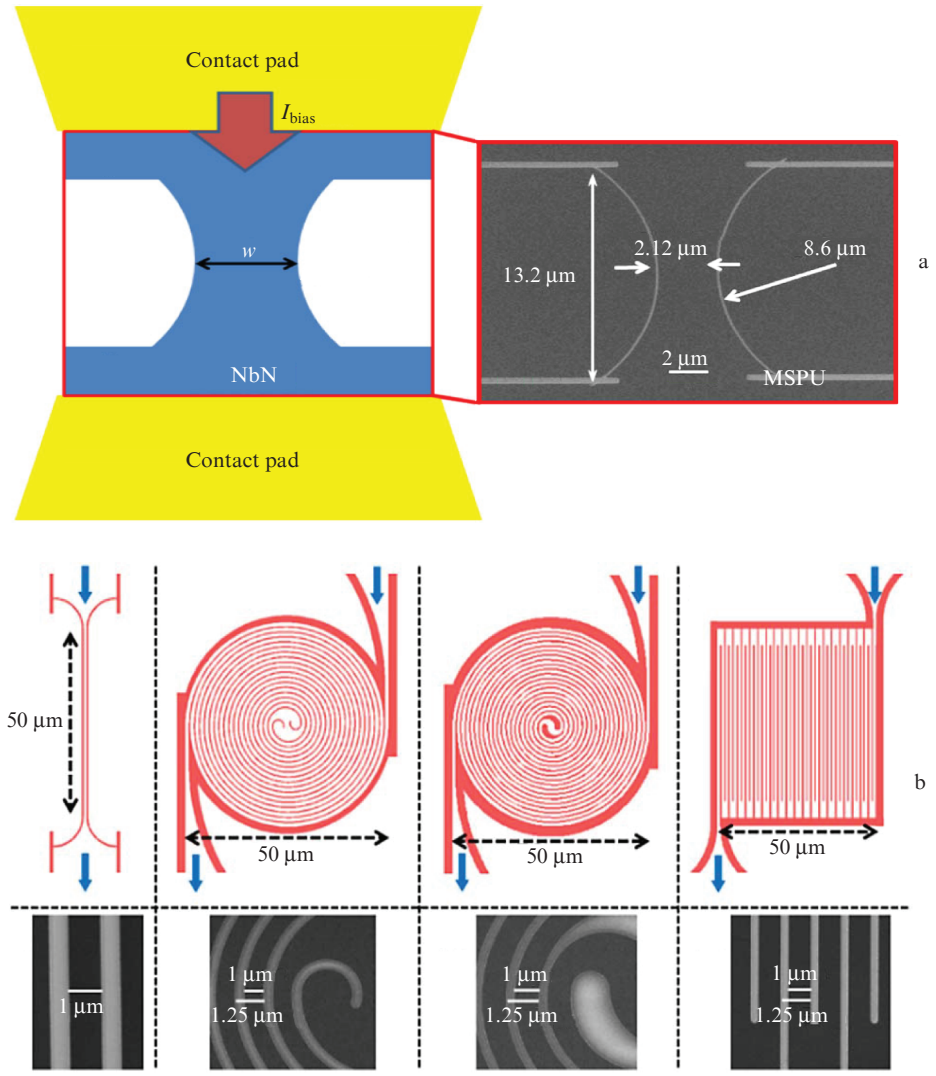

Figure 5. Structures of active elements of SMSPDs: (a) microbridge [25] and (b) microbridge, spiral and meander [59].

A microwire SMSPD has the following advantages over an SNSPD.

1. An SMSPD is produced using a photolithographic setup instead of an electron-beam lithography setup required to fabricate an SNSPD. This is due to lower requirements for the dimensional accuracy of the elements being made. Photolithography as a technological process is more stable and productive than electron-beam lithography, which will make it possible to significantly reduce the cost of producing one sensitive element of the detector and achieve repeatability, as well as will allow one to fabricate multi-pixel detectors with approximately the same sensitivity parameters of individual pixels.

2. An SMSPD for QKD application can make use of a microbridge topology; however, it is also necessary to use 'lensing' of the radiation emerging from the optical fibre to form a beam with a diameter equal to the width of the microwire. The use of a microbridge will significantly reduce the kinetic inductance of the detector in comparison with the meander topology and, accordingly, will reduce the dead time of the detector down to hundreds of picoseconds. In this case, the capacity of the cooling system will be the limiting factor. The latching effect will also have a stronger impact. Such a decrease in the dead time will significantly increase the rate of generation of the secret key in the QKD installation when using this type of detectors. If we assume that it is possible to create an SMSPD with a dead time $\tau = 100$ ps, then its limiting count rate will be 10 GHz, which will require significant improvement of the existing QKD devices for the most efficient use of an SPD.

Figure 5 shows SMSPD structures, where the active element is a microbridge from [25] or a microbridge, a spiral, and meander from [59].

Since the SMSPD device was first produced only in 2018, this technology is not yet fully developed, but very promising due to a significant simplification of the production process in comparison with the production of SNSPD nanowires. Thus, it can be expected that in the next few years there will be samples of SMSPDs that will surpass SNSPDs in their characteristics.

The currently achieved SNSPD and SMSPD characteristics based on various materials are presented in Table 1.

3. SPDs based on single-photon avalanche diodes

The structure of a single-photon avalanche diode (SPAD) was obtained by optimising the structure of an avalanche photodi-

Table 1. Characteristics of SNSPDs and SMSPDs (marked with *) according to review [34] and current data ($\lambda = 1310-1550$ nm).

Material	Thickness/nm	η_{sde} (%)	DCR/Hz	Jitter/ps	τ/ns	References
NbN	7		10^2	68–110	32	2017 [60]
	7	90–92	10^1	79	48.5	2017 [61]
	5–6			14.2		2017 [62]
	5.8*	~20*	10*			2018 [25]
	7	80	0.5			2018 [37]
	7	94				2018 [63]
	7			2.7–4.6		2018 [64]
	6.5	70	10^2	176	5.6	2018 [65]
	7	85	10^{-1}			2018 [37]
	5	68	200			2019 [66]
	6	98	100	66	42	2020 [44]
		94–99.5		15–26	33	2020 [67]
	7*	92.2*	200*	48*		2021 [59]
NbTiN	9	86		10.91		2017 [68]
	5	77.5	10^2	38–46	17	2017 [60]
	8.4	91.5–93.3	10^2	49	20	2017 [68]
		60 ± 3	220	45	4	2020 [45]
	8–11	80–90		7–16		2020 [69]
WSi	4–5	93	10^3	150	40	2013 [70]
	4.6	78 (70)	10^2 (1)	191 (225)		2014 [71]
	5	88		60		2014 [72]
MoSi	4	18	10^1	120	6	2014 [73]
	6.6	87.1	10^2	76	35	2015 [74]
	10	5	10^1	51		2016 [75]
		20	10^2			2017 [76]
	< 10	98				2020 [77]
	3*		10^{3*}			2020 [58]
MoGe	7.5	25– 30	10^2	69	9	2014 [78]
MoN	3.6				5	2017 [79]
NbN/αW_5Si_3	2/2	96	10^3	52	5	2017 [80]

ode (APD) for operation in the Geiger mode, i.e., a mode in which a bias voltage exceeding the breakdown voltage is applied to the diode. This mode is unstable, and even one charge carrier may be sufficient for the formation of a self-sustaining avalanche process (positive feedback). APDs usually operate in a linear mode, that is, absorbed photons generate electron–hole pairs, which subsequently lead to the formation of a finite number of charge carriers due to the avalanche multiplication process. In this case, the process is not self-sustaining, although it leads to signal amplification (positive feedback is replaced by negative feedback) [81]. Figure 6 schematically shows regions of APD operation and SPAD operation in the reverse current–voltage characteristics (I–V characteristics) [82]. Here U_{br} denotes the breakdown voltage, that is, the voltage above which avalanche processes are self-sustaining. When the bias voltage rises sufficiently quickly to U_a, breakdown does not occur immediately (position Off in the figure), and at this moment the diode is capable of detecting single photons. After a while, even without an initiating photon, the diode remains in the On-state (position On), which is characterised by large flowing currents (in the milliampere range).

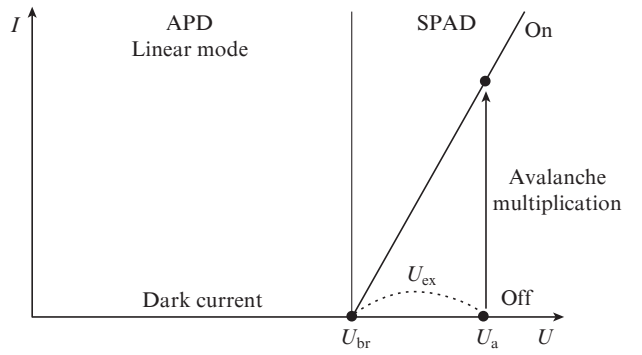

Figure 6. Regions of APD operation and SPAD operation in the reverse I–V characteristics [82]; $U_{ex} = U_a - U_{br}$ is the excess voltage.

The following types of structures are distinguished: separated absorption multiplication (SAM) [83], separated absorption charge multiplication (SACM) [84], and separated absorption grading charge multiplication (SAGCM) [85]. The structure of the SAGCM type is the most promising, since the best performance characteristics of diodes were achieved on it.

Depending on the type of carriers used in avalanche generation (electrons or holes), the order of the corresponding regions will also differ. Currently, SPADs based on InGaAs/InP structures [86–88], as well as InGaAs/InAlAs [89–91] and Si/Ge [92, 93] structures are used in quantum communications (λ = 1310 and 1550 nm). However, InGaAs/InAlAs and Si/Ge diodes have some problems, which currently does not allow them to compete with InGaAs/InP diodes.

For example, SPADs based on InGaAs/InAlAs structures are characterised by a high level of noise and there is a high probability of afterpulses compared to SPADs based on InGaAs/InP structures. In SPADs based on Si/Ge, sufficiently low noise levels can be achieved by cooling the diode to a temperature below –150 °C, which is rather difficult to implement using Peltier elements and a cooling system based on a Stirling engine [94]. As a consequence, these SPDs have larger dimensions than SPDs based on the so-called III–V materials.

To produce SPADs with the best parameters, their structures are optimised using simulation methods: models for InGaAs/InP diodes are presented in [95, 96], and models for InGaAs/InAlAs diodes are demonstrated in [97–99]. Diodes based on these structures are also used in classical communication optical networks [100, 101], but the parameters of the semiconductor layers in this case are very different. Examples of a structure of a front- and back-illuminated InGaAs/InP-based SPAD are shown in Fig. 7.

The schemes shown in Fig. 7 show a structure of the SAGCM type. The absorption region is made of $In_{0.53}Ga_{0.48}As$, the band gap is $\Delta E_g \approx 0.75$ eV at $T = 300$ K. It is important to note that the photon energy at $\lambda = 1550$ nm is approximately 0.8 eV. Thus, this material absorbs such photons well [96].

An important parameter of the multiplication region is the ratio of the ionisation coefficients for electrons and holes: α and β, respectively. For example, for InP the ratio is $\alpha/\beta \approx 0.25$ [103]. For this reason, the structures in Fig. 7 are designed in such a way that holes are the main carriers involved in impact ionisation. In InAlAs, the ratio of the ionisation coefficients is $\alpha/\beta \approx 1$ [99]; accordingly, the InGaAs/InAlAs SPAD structure is designed so that an electron initiates an avalanche response.

Let us consider in more detail the processes occurring in a front-illuminated InGaAs/InP diode (Fig. 7a). The active part of the structure is a cylinder 25 μm in diameter, which makes it possible to simplify the alignment of the position of the optical fibre in the diode housing and not to use microlenses. To reduce the probability of photon reflection, an antireflection coating is deposited on the structure.

The photon travels through multiplication, charge and transition regions. The probability of a photon being absorbed in these regions is rather small, since the band gap of InP, of which they are made, is greater than the photon energy. Nevertheless, phonon scattering is still present, which leads to a decrease in the overall detection efficiency. The photon enters the absorption region and is absorbed with a high probability with the formation of an electron–hole pair. Then, charge carriers are separated: the electron 'flows down' to the n-metallisation layer, and the hole moves towards the p-contact. The transition region makes it possible to reduce the heterobarrier at the InGaAs–InP interface. It usually consists of an InGaAsP quaternary alloy, in which the concentration of P increases towards the charge region, while the concentration of GaAs, on the contrary, decreases. The charge region is used to control the field strength in the absorption and multiplication regions. Thus, the field in the absorption region should be small, and in the multiplication region – high and uniform along the entire length of the layer. In the multiplication region, avalanche multiplication of the primary charge of the hole occurs with the formation of a large number of electron–hole pairs. It is important to note that electrons are also involved in the avalanche formation. If the bias voltage across the diode exceeds U_{br}, then the resulting avalanche will be self-sustaining; however, the diode remains in this mode too long, the heterostructure is irreversibly destructed.

In the back-illuminated SPAD structure (Fig. 7b), the purpose of all layers is similar. However, in this design, the photon immediately enters the absorption region, without passing through the multiplication, transition and charge regions.

The advantage of back-illuminated SPADs is that the probability of photon scattering is lower than in front-illuminated SPADs, since the photon does not travel 'extra' dis-

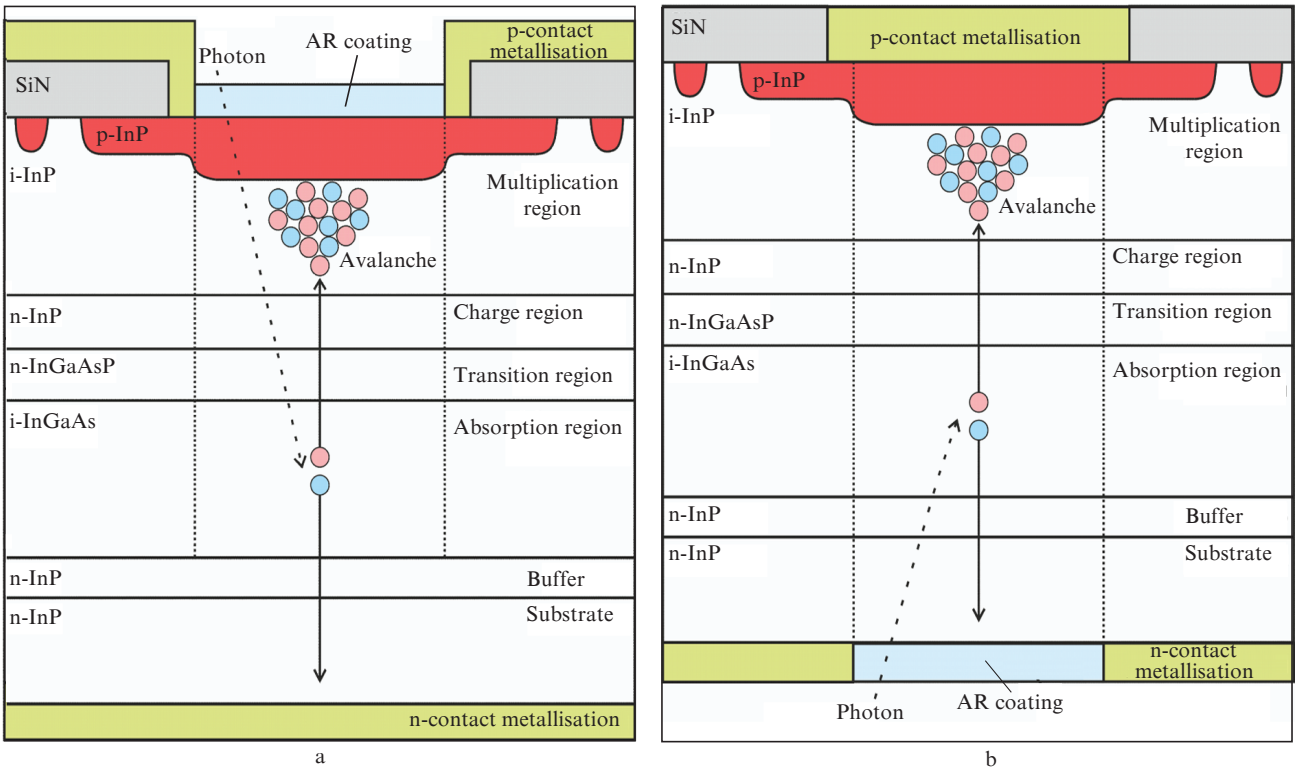

Figure 7. (a) Front-illuminated [96] and (b) back-illuminated [102] SPADs based on InGaAs/InP structures.

tances in the material in which it cannot generate an electron–hole pair. However, the timing jitter in the front-illuminated structure is less than in the back-illuminated structure, since the initial electron–hole pair is most likely generated close to the multiplication region and the time of carrier transfer to the multiplication region is rather short.

The external photon detection efficiency η_{sde} for diodes based on III–V heterostructures is about 70% [104], while Si diodes make it possible to achieve $\eta_{sde} > 90\%$ for visible radiation [105, 106]. This is due to the fact that structures made of materials of III–V groups still have significantly higher defect concentrations than structures made of Si. With the development of technologies for deposition of III–V heterostructures, the parameters of SPADs based on them will be able to approach the parameters obtained for diodes made of Si.

Consider the noise processes occurring in SPADS. As noted in Section 2, SPADs have some correlations between the trigger probability the current moment of time and previous triggers [107]. This effect is called afterpulsing [108]. After the self-sustaining avalanche is interrupted by the control electronics, a large number of filled electron and hole traps remain in the structure. The nature of these traps is associated with dopant ions and crystal lattice defects (especially at heterojunctions). Thus, at the next transition of the diode to the Geiger mode, there is a high probability of the detector triggering precisely due to the relaxation of charges from the traps with the subsequent development of the avalanche process. It is impossible to get rid of this effect completely, but one can significantly minimise its impact. For example, if a dead time is introduced for the detector, during which the diode will transit to a linear mode, then the relaxation of the traps will not lead to triggers, since the avalanche processes will not be self-sustaining [109]. The second option is to increase the operating temperature of the diode, since the processes of relaxation of charges from traps are associated with phonon interactions. This makes it possible to significantly reduce their relaxation time [110]. The third method is to accelerate the quenching of the avalanche process to minimise the charge flowing through the structure, which leads to a decrease in the concentration of filled traps in the heterostructure. In this case, active quenching schemes [111] and high-frequency gating [112] are used.

There are other processes that lead to dark responses of the detectors. For example, thermal generation (SRH recombination) and band-to-band tunnelling are the main sources of detector noise [96]. To reduce the effect of thermal generation, it is necessary to reduce the operating temperature of the diode. However, this will increase the likelihood of afterpulses. To minimise the effect of band-to-band tunnelling, it is possible to reduce the field strength in the main regions of the device structure, but this will also decrease the photon detection efficiency. Accordingly, for the effective operation of an SPD as a whole, it is necessary to find some optimal combination of both the parameters of the structure of the device and its control parameters, which is a nontrivial task.

Acerbi et al. [96] studied theoretically the SPAD parameters at various parameters of structures and experimentally validated the found regularities. The authors showed that thermal generation is dominant at temperatures above 250 K for narrow multiplication regions (width $w_m < 1$ μm) and at temperatures above 200 K for wide multiplication regions with $w_m > 2$ μm. In this case, band-to-band charge generation makes a much smaller contribution and, on the whole, is less dependent on temperature. It was also shown that with an increase in the excess voltage on the diode $U_{ex} = U_a - U_{br}$, the photon detection efficiency η_{sde} increases, with the DCR noise level also increasing. This is due to the fact that an increase in the excess voltage leads to an increase in the probability of

avalanche excitation by a single charge, and also increases the probability of band-to-band tunnelling. In this case, thermal generation is a certain constant component, and band-to-band generation increases. An important result of the work was the proof that with wider multiplication regions, lower noise levels are observed with a similar efficiency.

Thus, for more efficient SPAD operation, it is necessary that the multiplication region width w_m be large enough – more than 2 μm. This is the main difference between APDs and SPADs: APDs are designed with a sufficiently small width of the multiplication region (less than 0.5 μm) to minimise the dead space effect influence [113] and control the number of charges generated by the initial charge [114]. Thus, SPADs can indeed be classified as a new class of semiconductor devices, since the parameters of their structures differ significantly from the parameters of APD structures and they are intended for solving completely different problems.

In addition to the linear and Geiger modes of APD and SPAD operation, there are also gated [115] and free-running [116] modes. The gated mode of operation assumes a periodic transition of the diode to the Geiger mode under the action of a certain gating signal (it can be, for example, rectangular pulses or a sinusoidal signal). The free-running mode of operation assumes that the diode is in the Geiger mode until its avalanche breakdown occurs. The advantage of the gated mode of operation is the low DCR and afterpulse values compared to the free-running mode, while the disadvantages are the need to design more complex control electronics and the problems associated with synchronisation of the gating signal and optical radiation. Thus, the advantage of the free-running mode is simpler electronics, the absence of the need for synchronisation with an optical signal and, as a consequence, the possibility of using it for a wider range of tasks; the disadvantages of this mode include high values of noise and afterpulses, as well as a long dead time τ [117].

Gated-mode SPDs based on SPADs are more suitable for use in QKD systems than free-running-mode SPDs, since the key distribution protocol already assumes the presence of synchronisation. Free-running-mode detectors are more suitable for microscopy, OTDR, LIDAR applications. It is also necessary to distinguish between the problems of key distribution at short and long distances, since the requirements for the detector will differ in this case. For key generation at short distances (within the same city or building), the DCR value does not have a large effect on the key generation rate, while the photon detection efficiency and dead time are more important parameters. This is due to the fact that a small number of photons are absorbed in the communication line, and it is more expedient to maximise their detection efficiency and minimise losses due to the finite dead time. The opposite situation occurs when generating a key over long distances (long-distance communications). In this case, the loss in the communication line is so great that the key generation rate can drop to several kbit s^{-1} [118]. In this case, it is advisable to strive for a decrease in DCR and the probability of afterpulses.

The achieved to date characteristics of SPDs based on SPADs with different structures are presented in Table 2.

Table 2. SPD characteristics based on SPADs ($\lambda = 1310-1550$ nm); f_g is the gating frequency.

Material	η_{sde} (%)	DC/Hz	Afterpulse probability (%)	τ/μs	Temperature/K	References
InGaAs/InP	10.4	$f_g \cdot 6.4 \times 10^{-7}$	1.6		223	2010 [119]
	10.5	$f_g \cdot 6.1 \times 10^{-7}$	3.4		223	
	10.0	1	2.2	20	163	2014 [120]
	50	$f_g \times 10^{-4}$	7		293	2015 [121]
	55	$f_g \times 10^{-4}$	10.2	10^{-2}	293	
	27.5	1200	9.1	0.1	223	2017 [87]
	10	$f_g \cdot 1.6 \times 10^{-6}$	3.3	0.1	223	
	10.6	$f_g \cdot 2.5 \times 10^{-5}$	1.3	10^{-3}	294	2018 [88]
	23.6	$f_g \cdot 7.7 \times 10^{-5}$	3.4	10^{-3}	293	
	60	340×10^3	14.8		300	2020 [122]
	40	3000	5.5		253	
	55.9	$f_g \cdot 4.7 \times 10^{-4}$	5	0.2	289	2020 [123]
	52.4	$f_g \cdot 3.1 \times 10^{-4}$	0	0.2	289	
	27.7	$f_g \cdot 8 \times 10^{-7}$	1.8	0.2	238	
	48.0	$f_g \cdot 8.9 \times 10^{-6}$	12.9	0.2	238	
	70.0	48×10^3	> 2.2		233	2020 [104]
	55.0	20×10^3	1.6		233	
InGaAs/InAlAs	10.0	$\sim 10^8$			290	2014 [89]
	21.0	$\sim 10^8$			260	
	26.0	$\sim 10^8$			210	2016 [90]
	32.0		< 1	2	200	2020 [91]
Si/Ge	38.0		1	1	125	2019 [92]
	38.0		0.1	10	125	
	29.4	$< 10^5$			125	2020 [93]

4. Comparison of two types of SPDs

The review considers physical processes, various types of structures, emerging problems and methods for their solution for two types of detectors designed for detecting photons with $\lambda = 1310/1550$ nm, that is, detectors based on superconducting nanowires (SNSPD and SMSPD) and detectors based on a single-photon avalanche diode.

To design a compact (suitable for a standard server rack) QKD system, it is necessary to use an SPD based on an InGaAs/InP SPAD. This is primarily due to the achieved overall dimensions of these detectors. For them, it is possible to use multistage Peltier elements for cooling the diode, since the required temperatures are in the range from –60 °C to –40 °C. ID Quantique uses a Stirling engine cooling system for its detectors to achieve temperatures as close to –110 °C; in this case, the following values can be obtained for the detector parameters: DCR ≈ 20 Hz, PDE ≈ 10% [124]. However, the dimensions of this device, as a rule, are much larger, and the cost is much higher. In some SPAD designs, the Peltier elements and the diode structure are located in the same housing, which makes it possible to further reduce the overall dimensions of the detector.

For an industrial QKD system connecting two points at a distance of more than 100 km, it is more expedient to use SNSPDs [125]. This is due to the fact that, due to attenuation in the line, a small number of photons arrive at the detector, and even low noise characteristics lead to a high value of the quantum bit error rate (QBER) parameter – an indicator of the security of the generated key. SPDs based on SPADs can be used at distances less than 100 km, which will significantly reduce the cost of the entire QKD system, but the key generation rate will be much lower than in the case of SNSPDs [126, 118].

In a QKD system designed to generate a key within the same city or even one building, a detector with the highest PDE should be used. In this case, the line attenuation is low enough, and a high signal level can be obtained even with a high noise level. Thus, an SPD can be used both based on any SPAD type (however, diodes with an InGaAs/InP structure are preferable) and based on SNSPDs.

When implementing a star topology, in which multiple laser transmitters are connected to a single receiver, it is more appropriate to use SNSPDs. This is due to the fact that there is a sequential switching of the receiver input from one transmitter to another, and the permissible period of operation of one pair is very limited. In a short period of time, it is necessary to generate a certain information volume of the secret key. With a small number of users (less than five), the requirements for PDE and noise performance of SPDs are not as stringent as with a large number of users. To build a single network with more than 20 users, SNSPDs should be used exclusively [127].

The advantages of an SPD based on an SPAD are obviously its small size and cost. It is more expedient to use such a detector in optical time-domain reflectometry (OTDR) [128], as well as in 3D imaging LIDARs [129]. The high efficiency of photon detection and low noise level in SNSPDs makes their use more expedient in an optical quantum computer [130], astronomical telescope [131]. In addition, there are areas such as fluorescence microscopy [132], tomography of biomarkers [133], etc., in which both detectors can be effectively used.

In 2016 an SNSPD was used to achieve a record for the terrestrial key transmission distance of 404 km using the decoy-state MDIQKD protocol [134]. In this case, an optical fibre with a low attenuation coefficient (0.16 dB km^{-1} at a wavelength of 1550 nm) was used, the quantum key generation rate was 1.15 bit h^{-1}, and the authors took three months to generate 2584 bits.

The use of twin-field technology, in which there is a trusted relay node between two users, allowed Chen et al. to achieve in 2020 a record for the key transmission distance of 509 km [135], which is more than 100 km higher than the record for key transmission exclusively between two users.

QKD systems allow achieving a greater range of action when using information transmission in open space. In 2017, five achievements in the field of QKD were presented: 'ground-to-aircraft' [136] and 'satellite-to-ground' QKD systems [137, 138], the distribution of entangled states using a satellite over a distance of more than 1200 km [139], and teleportation single photonic earth-satellite qubits at a distance of up to 1400 km [140]. Finally, in 2018, Liao and his colleagues [141] successfully implemented a QKD system with entangled states between a satellite in low orbit and several ground stations separated by 7600 km. Thus, significant steps have been taken towards the implementation of quantum networks over long distances.

Acknowledgements. This work was supported by the Russian Science Foundation (Grant No. 17-71-20146).

References

1. Babash A., Baranova E. *Kriptograficheskie metody zashchity informatsii: uchebnik dlya vuzov* (Cryptographic Methods of Information Protection: A Textbook for Universities) (Moscow: KnoRus, 2016).
2. Deng F.G., Long G.L. *Phys. Rev. A*, **69**, 052319 (2004).
3. Wu C.H., Hong J.-H., Wu C.-W. *Proc. 2001 Asia and South Pacific Design Automation Conf. (ASP-DAC)* (Yokohama, 2001) pp 391–395.
4. Yang C.-C., Chang T.-S., Jen C.-W. *IEEE Trans. on Circuits and Systems II: Analog and Digital Signal Processing*, **45** (7), 908 (1998).
5. Maurer U.M., Wolf S. *Designs, Codes and Cryptography*, **19** (2), 147 (2000).
6. Gupta S., Sharma J. *Proc. 2012 IEEE Int. Conf. on Computational Intelligence and Computing Research (ICCIC 2012)* (Coimbatore, India, 2012) pp 1 – 4.
7. Arute F., Arya K., Babbush R., Bacon D., Bardin J.C., Barends R., Biswas R., Boixo S., Brandao F.G., Buell D.A., et al. *Nature*, **574**, 505 (2019).
8. Zhong H.-S., Wang H., Deng Y.-H., Chen M.-C., Peng L.-C., Luo Y.-H., Qin J., Wu D., Ding X., Hu Y., et al. *Science*, **370**, 1460 (2020).
9. Ekert A., Jozsa R. *Rev. Mod. Phys.*, **68**, 733 (1996).
10. Zalka C. *Phys. Rev. A*, **60**, 2746 (1999).
11. Alani M.M. *Proc. 3rd Int. Conf. on Cryptography, Security and Privacy* (Kuala Lumpur, Malaysia, 2019) pp 23 – 27.
12. Bennett C.H., Brassard G. *Proc. IEEE Int. Conf. on Computers, Systems and Signal Processing* (Bangalore, 1984) pp 175 – 179.
13. Bennett C.H., Bessette F., Brassard G., Salvail L., Smolin J. *J. Cryptology*, **5** (1), 3 (1992).
14. Bedington R., Arrazola J.M., Ling A. *npj Quantum Inf.*, **3**, 30 (2017).
15. Toonabi A.M., Darareh M.D., Janbaz S. *Int. J. Quantum Inf.*, **17**, 1950058 (2019).
16. Miki S., Yamashita T., Fujiwara M., Sasaki M., Wang Z. *Opt. Lett.*, **35** (13), 2133 (2010).

17. Dutton N., Gyongy I., Parmesan L., Henderson R. *Sensors*, **16** (7), 1122 (2016).
18. Peacock A., Verhoeve P., Rando N., Van Dordrecht A., Taylor B., Erd C., Perryman M., Venn R., Howlett J., Goldie D., et al. *Nature*, **381**, 135 (1996).
19. Irwin K.D. *Appl. Phys. Lett*., **66**, 1998 (1995).
20. Day P.K., LeDuc H.G., Mazin B.A., Vayonakis A., Zmuidzinas J. *Nature*, **425**, 817 (2003).
21. Gol'tsman G., Okunev O., Chulkova G., Lipatov A., Semenov A., Smirnov K., Voronov B., Dzardanov A., Williams C., Sobolewski R. *Appl. Phys. Lett*., **79** (6), 705 (2001).
22. Verevkin A., Zhang J., Sobolewski R., Lipatov A., Okunev O., Chulkova G., Korneev A., Smirnov K., Gol'tsman G., Semenov A. *Appl. Phys. Lett*., **80** (25), 4687 (2002).
23. Zhang J., Boiadjieva N., Chulkova G., Deslandes H., Gol'Tsman G., Korneev A., Kouminov P., Leibowitz M., Lo W., Malinsky R., et al. *Electron. Lett*., **39** (14), 1086 (2003).
24. Natarajan C.M., Tanner M.G., Hadfield R.H. *Supercond. Sci. Technol*., **25** (6), 063001 (2012).
25. Korneeva Y.P., Vodolazov D.Y., Semenov A., Florya I., Simonov N., Baeva E., Korneev A., Goltsman G., Klapwijk T. *Phys. Rev. Appl*., **9** (6), 064037 (2018).
26. Florya I., Korneeva Y.P., Mikhailov M.Y., Devizenko A.Y., Korneev A., Goltsman G. *Low Temp. Phys*., **44** (3), 221 (2018).
27. Zadeh E.I., Chang J., Los J.W., Gyger S., Elshaari A.W., Steinhauer S., Dorenbos S.N., Zwiller V. *Appl. Phys. Lett*., **118** (19), 190502 (2021).
28. Engel A., Schilling A. *J. Appl. Phys*., **114** (21), 214501 (2013).
29. Engel A., Renema J., Il'in K., Semenov A. *Supercond. Sci. Technol*., **28** (11), 114003 (2015).
30. Likharev K. *Rev. Mod. Phys*., **51** (1), 101 (1979).
31. Liu D.-K., Chen S.-J., You L.-X., Wang Y.-L., Miki S., Wang Z., Xie X.-M., Jiang M.-H. *Appl. Phys. Express*, **5** (12), 125202 (2012).
32. Chiles J., Buckley S.M., Lita A., Verma V.B., Allmaras J., Korzh B., Shaw M.D., Shainline J.M., Mirin R.P., Nam S.W. *Appl. Phys. Lett*., **116** (24), 242602 (2020).
33. Ravindran P., Cheng R., Tang H., Bardin J.C. *Opt. Express*, **28** (3), 4099 (2020).
34. Holzman I., Ivry Y. *Adv. Quantum Technol*., **2** (3 – 4), 1800058 (2019).
35. Zhang H., Liu J., Guo J., Xiao L., Xie J. *Opt. Express*, **28** (11), 16696 (2020).
36. Korzh B., Zhao Q.-Y., Allmaras J.P., Frasca S., Autry T.M., Bersin E.A., Beyer A.D., Briggs R.M., Bumble B., Colangelo M., et al. *Nat. Photonics*, **14** (4), 250 (2020).
37. Zhang W., Yang X., Li H., You L., Lv C., Zhang L., Zhang C., Liu X., Wang Z., Xie X. *Supercond. Sci. Technol*., **31** (3), 035012 (2018).
38. Yang X., Li H., Zhang W., You L., Zhang L., Liu X., Wang Z., Peng W., Xie X., Jiang M. *Opt. Express*, **22** (13), 16267 (2014).
39. Zhang C., Zhang W., You L., Huang J., Li H., Sun X., Wang H., Lv C., Zhou H., Liu X., et al. *IEEE Photonics J*., **11** (5), (2019).
40. Schmidt E., Ilin K., Siegel M. *IEEE Trans. Appl. Supercond*., **27** (4), 1 (2016).
41. Wollman E.E., Verma V.B., Beyer A.D., Briggs R.M., Korzh B., Allmaras J.P., Marsili F., Lita A.E., Mirin R., Nam S., et al. *Opt. Express*, **25** (22), 26792 (2017).
42. Wein S.C., Ji J.-W., Wu Y.-F., Asadi F.K., Ghobadi R., Simon C. *Phys. Rev. A*, **102** (3), 033701 (2020).
43. Burenkov V., Xu H., Qi B., Hadfield R.H., Lo H.-K. *J. Appl. Phys*., **113** (21), 213102 (2013).
44. Hu P., Li H., You L., Wang H., Xiao Y., Huang J., Yang X., Zhang W., Wang Z., Xie X. *Opt. Express*, **28** (24), 36884 (2020).
45. Meng Y., Zou K., Hu N., Lan X., Xu L., Zichi J., Steinhauer S., Zwiller V., Hu X. *Opt. Lett*., **45** (2), 471 (2020).
46. Li D., Jiao R. *Photonics Res*., **7** (8), 847 (2019).
47. Chi X., Zou K., Gu C., Zichi J., Cheng Y., Hu N., Lan X., Chen S., Lin Z., Zwiller V., et al. *Opt. Lett*., **43** (20), 5017 (2018).
48. Zhang W., Huang J., Zhang C., You L., Lv C., Zhang L., Li H., Wang Z., Xie X.A. *IEEE Trans. Appl. Supercond*., **29** (5), 1 (2019).
49. Allmaras J.P., Wollman E.E., Beyer A.D., Briggs R.M., Korzh B.A., Bumble B., Shaw M.D. *Nano Lett*., **20** (3), 2163 (2020).
50. Yamashita T., Miki S., Terai H., Wang Z. *Opt. Express*, **21** (22), 27177 (2013).
51. Miki S., Yamashita T., Terai H., Wang Z. *Opt. Express*, **21** (8), 10208 (2013).
52. Li H., Zhang L., You L., Yang X., Zhang W., Liu X., Chen S., Wang Z., Xie X. *Opt. Express*, **23** (13), 17301 (2015).
53. Li D., Liu X., Jiao R. *AIP Adv*., **10** (8), 085111 (2020).
54. Munzberg J., Vetter A., Beutel F., Hartmann W., Ferrari S., Pernice W.H., Rockstuhl C. *Optica*, **5** (5), 658 (2018).
55. You L., Li H., Zhang W., Yang X., Zhang L., Chen S., Zhou H., Wang Z., Xie X. *Supercond. Sci. Technol*., **30** (8), 084008 (2017).
56. Vodolazov D.Y. *Phys. Rev. Appl*., **7** (3), 034014 (2017).
57. Manova N., Smirnov E.O., Korneev A., Goltsman G., et al. *J. Phys.: Conf. Series*, **1410**, 012147 (2019).
58. Charaev I., Morimoto Y., Dane A., Agarwal A., Colangelo M., Berggren K.K. *Appl. Phys. Lett*., **116** (24), 242603 (2020).
59. Xu G.-Z., Zhang W.-J., You L.-X., Xiong J.-M., Sun X.-Q., Huang H., Ou X., Pan Y.-M., Lv C.-L., Li H., et al. *Photonics Res.,* **9** (6), 958 (2021).
60. Yang X., You L., Zhang L., Lv C., Li H., Liu X., Zhou H., Wang Z. *IEEE Trans. Appl. Supercond*., **28** (1), 1 (2017).
61. Zhang W., You L., Li H., Huang J., Lv C., Zhang L., Liu X., Wu J., Wang Z., Xie X. *Science China: Physics, Mechanics & Astronomy*, **60** (12), 1 (2017).
62. Wu J., You L., Chen S., Li H., He Y., Lv C., Wang Z., Xie X. *Appl. Opt*., **56** (8), 2195 (2017).
63. Smirnov K., Divochiy A., Vakhtomin Y., Morozov P., Zolotov P., Antipov A., Seleznev V. *Supercond. Sci. Technol*., **31** (3), 035011 (2018).
64. Miki S., Miyajima S., Yabuno M., Yamashita T., Yamamoto T., Imoto N., Ikuta R., Kirkwood R., Hadfield R., Terai H. *Appl. Phys. Lett*., **112** (26), 262601 (2018).
65. Huang J., Zhang W., You L., Zhang C., Lv C., Wang Y., Liu X., Li H., Wang Z. *Supercond. Sci. Technol*., **31** (7), 074001 (2018).
66. Tao X., Chen S., Chen Y., Wang L., Li X., Tu X., Jia X., Zhao Q., Zhang L., Kang L., et al. *Supercond. Sci. Technol*., **32** (6), 064002 (2019).
67. Chang J., Los J.W.N., Tenorio-Pearl J.O., Noordzij N., Gourgues R., Guardiani A., Zichi J.R., Pereira S.F., Urbach H.P., Zwiller V., Dorenbos S.N., Zadeh I.E. arXiv: 2011.08941v1, 2020.
68. Zadeh E.I., Los J.W., Gourgues R.B., Steinmetz V., Bulgarini G., Dobrovolskiy S.M., Zwiller V., Dorenbos S.N. *Appl. Photonics*, **2** (11), 111301 (2017).
69. Zadeh E.I., Los J.W., Gourgues R.B., Chang J., Elshaari A.W., Zichi J.R., van Staaden Y.J., Swens J.P., Kalhor N., Guardiani A., et al. *ACS Photonics*, **7** (7), 1780 (2020).
70. Marsili F., Verma V.B., Stern J.A., Harrington S., Lita A.E., Gerrits T., Vayshenker I., Baek B., Shaw M.D., Mirin R.P., et al. *Nat. Photonics*, **7** (3), 210 (2013).
71. Verma V.B., Korzh B., Bussieres F., Horansky R.D., Lita A.E., Marsili F., Shaw M., Zbinden H., Mirin R., Nam S. *Appl. Phys. Lett*., **105** (12), 122601 (2014).
72. Dauler E.A., Grein M.E., Kerman A.J., Marsili F., Miki S., Nam S.W., Shaw M.D., Terai H., Verma V.B., Yamashita T. *Opt. Eng*., **53** (8), 081907 (2014).
73. Korneeva Y.P., Mikhailov M.Y., Pershin Y.P., Manova N., Divochiy A., Vakhtomin Y.B., Korneev A., Smirnov K., Sivakov A., Devizenko A.Y., et al. *Supercond. Sci. Technol*., **27** (9), 095012 (2014).
74. Verma V.B., Korzh B., Bussieres F., Horansky R.D., Dyer S.D., Lita A.E., Vayshenker I., Marsili F., Shaw M.D., Zbinden H., et al. *Opt. Express*, **23** (26), 33792 (2015).
75. Li J., Kirkwood R.A., Baker L.J., Bosworth D., Erotokritou K., Banerjee A., Heath R.M., Natarajan C.M., Barber Z.H., Sorel M., et al. *Opt. Express*, **24** (13), 13931 (2016).
76. Caloz M., Korzh B., Timoney N., Weiss M., Gariglio S., Warburton R.J., Schonenberger C., Renema J., Zbinden H., Bussieres F. *Appl. Phys. Lett*., **110** (8), 083106 (2017).

77. Reddy D.V., Nerem R.R., Nam S.W., Mirin R.P., Verma V.B. *Optica*, **7** (12), 1649 (2020).
78. Verma V.B., Lita A.E., Vissers M.R., Marsili F., Pappas D.P., Mirin R.P., Nam S.W. *Appl. Phys. Lett*., **105** (2), 022602 (2014).
79. Korneeva Y., Florya I., Vdovichev S., Moshkova M., Simonov N., Kaurova N., Korneev A., Goltsman G. *IEEE Trans. Appl. Supercond*., **27** (4), 1 (2017).
80. Ivry Y., Surick J.J., Barzilay M., Kim C.-S., Najafi F., Kalfon-Cohen E., Dane A.D., Berggren K.K. *Nanotechnol.*, **28** (43), 435205 (2017).
81. Donati S., Tambosso T. *IEEE J. Sel. Top. Quantum Electron*., **20** (6), 204 (2014).
82. Cova S., Ghioni M., Lotito A., Rech I., Zappa F. *J. Mod. Opt*., **51** (9 – 10), 1267 (2004).
83. Cheong J.S., Ong J.S.L., Ng J.S., Krysa A.B., David J.P. *IEEE J. Sel. Top. Quantum Electron*., **20** (6), 142 (2014).
84. Zarifkar A., Soroosh M. *Proc. 6th Int. Conf. on Laser and Fiber-Optical Networks Modeling (LFNM) 2004* (Kharkiv, Ukraine, 2004) pp 213–219.
85. Zhao Y. *IEEE Trans. Electron Devices*, **60** (10), 3493 (2013).
86. Tosi A., Acerbi F., Anti M., Zappa F. *IEEE J. Quantum Electron*., **48** (9), 1227 (2012).
87. Jiang W.-H., Liu J.-H., Liu Y., Jin G., Zhang J., Pan J.-W. *Opt. Lett*., **42** (24), 5090 (2017).
88. Chen H., Jiang M., Sun S., Tang G., Liang L. *AIP Adv*., **8** (7), 075106 (2018).
89. Meng X., Tan C.H., Dimler S., David J.P., Ng J.S. *Opt. Express*, **22** (19), 22608 (2014).
90. Meng X., Xie S., Zhou X., Calandri N., Sanzaro M., Tosi A., Tan C.H., Ng J.S. *R. Soc. Open Sci.*, **3** (3), 150584 (2016).
91. Lee Y.-S., Chen Y.-J., Wu P.-L., Shi J.-W., et al. *Proc. 2020 CLEO: Applications and Technology* (San Jose, USA, 2020) paper AF1I.8.
92. Kirdoda J., Dumas D.C., Millar R.W., Mirza M.M., Paul D.J., Kuzmenko K., Vines P., Greener Z., Buller G.S. *Proc. 2019 IEEE 2nd British and Irish Conf. on Optics and Photonics (BICOP)* (London, 2019) pp 1 – 4.
93. Llin L.F., Kirdoda J., Thorburn F., Huddleston L.L., Greener Z.M., Kuzmenko K., Vines P., Dumas D.C., Millar R.W., Buller G.S., et al. *Opt. Lett*., **45** (23), 6406 (2020).
94. Vines P., Kuzmenko K., Kirdoda J., Dumas D.C., Mirza M.M., Millar R.W., Paul D.J., Buller G.S. *Nat. Commun*., **10** (1), 1 (2019).
95. Lee K., Yang K. *IEEE Photonics Technol. Lett*., **26**, 999 (2014).
96. Acerbi F., Anti M., Tosi A., Zappa F. *IEEE Photonics J*., **5** (2), 6800209 (2013).
97. Chen J., Zhang Z., Zhu M., Xu J., Li X. *Nanoscale Res. Lett*., **12** (1), 33 (2017).
98. Cao S., Zhao Y., Feng S., Zuo Y., Zhang L., Cheng B., Li C. *Nanoscale Res. Lett*., **14** (1), 3 (2019).
99. Cao S., Zhao Y., ur Rehman S., Feng S., Zuo Y., Li C., Zhang L., Cheng B., Wang Q. *Nanoscale Res. Lett*., **13** (1), 158 (2018).
100. Ren M., Gu X., Liang Y., Kong W., Wu E., Wu G., Zeng H. *Opt. Express*, **19** (14), 13497 (2011).
101. Liu J.-J., Ho W.-J., Chen J.-Y., Lin J.-N., Teng C.-J., Yu C.-C., Li Y.-C., Chang M.-J. *Sensors*, **19** (15), 3399 (2019).
102. Wang C., Wang J., Xu Z., Wang R., Li J., Zhao J., Wei Y., Lin Y. *Optik*, **185**, 1134 (2019).
103. Kao C.-W., Crowell C. *Solid-State Electron*., **23** (8), 881 (1980).
104. Zhou M., Wang W., Qu H., Han H., Zhu Y., Guo Z., Gui L., Wang X., Lu W. *Opt. Quantum Electron*., **52**, 1 (2020).
105. Bronzi D., Villa F., Tisa S., Tosi A., Zappa F. *IEEE Sens. J*., **16** (1), 3 (2016).
106. Zang K., Jiang X., Huo Y., Ding X., Morea M., Chen X., Lu C.-Y., Ma J., Zhou M., Xia Z., et al. *Nat. Commun*., **8** (1), 1 (2017).
107. Wang F.-X., Chen W., Li Y.-P., He D.-Y., Wang C., Han Y., Wang S., Yin Z., Li H.-W. *J. Lightwave Technol*., **34** (15), 3610 (2016).
108. Bronzi D., Tisa S., Villa F., Bellisai S., Tosi A., Zappa F. *IEEE Photonics Technol. Lett*., **25** (8), 776 (2013).
109. Ziarkash A.W., Joshi S.K., Stipcevic M., Ursin R. *Sci. Rep*., **8** (1), 1 (2018).
110. Itzler M.A., Jiang X., Entwistle M. *J. Mod. Opt*., **59** (17), 1472 (2012).
111. Ceccarelli F., Acconcia G., Gulinatti A., Ghioni M., Rech I. *IEEE Photonics Technol. Lett*., **31** (1), 102 (2018).
112. Jiang W.-H., Gao X.-J., Fang Y.-Q., Liu J.-H., Zhou Y., Jiang L.-Q., Chen W., Jin G., Zhang J., Pan J.-W. *Rev. Sci. Instrum*., **89** (12), 123104 (2018).
113. Tan L., Ng J., Tan C., David J. *IEEE J. Quantum Electron*., **44** (4), 378 (2008).
114. Ng J., Tan C., David J., Rees G. *IEEE J. Quantum Electron*., **41** (8), 1092 (2005).
115. Berdalovic I., Osrecki Z., Segmanovic F., Grubisic D., Knezevic T., Suligoj T. *Proc. 2016 39th Int. Convention on Information and Communication Technology, Electronics and Microelectronics (MIPRO)* (Opatija, Croatia, 2016) pp 34 – 39.
116. Liu J., Li Y., Ding L., Wang Y., Zhang T., Wang Q., Fang J. *IEEE J. Quantum Electron*., **52** (10), 1 (2016).
117. Maddox S.J., Ren M., Woodson M.E., Bank S.R., Campbell J.C. *Proc. SPIE, Image Sensing Technologies: Materials, Devices, Systems and Applications III*, **9854**, 985405 (2016).
118. Zhang Q., Xu F., Chen Y.-A., Peng C.-Z., Pan J.-W. *Opt. Express*, **26** (18), 24260 (2018).
119. Namekata N., Adachi S., Inoue S. *IEEE Photonics Technol. Lett*., **22** (8), 529 (2010).
120. Korzh B., Walenta N., Lunghi T., Gisin N., Zbinden H. *Appl. Phys. Lett*., **104** (8), 081108 (2014).
121. Comandar L.C., Frohlich B., Dynes J.F., Sharpe A.W., Lucamarini M., Yuan Z., Penty R.V., Shields A.J. *J. Appl. Phys*., **117** (8), 083109 (2015).
122. Fang Y.-Q., Chen W., Ao T.-H., Liu C., Wang L., Gao X.-J., Zhang J., Pan J.-W. *Rev. Sci. Instrum*., **91** (8), 083102 (2020).
123. Tada A., Namekata N., Inoue S. *Japan. J. Appl. Phys*., **59** (7), 072004 (2020).
124. https://www.idquantique.com/quantum-sensing/products/infrared_photon_counters, may 2021.
125. Wang S., Chen W., Yin Z.-Q., Li H.-W., He D.-Y., Li Y.-H., Zhou Z., Song X.-T., Li F.-Y., Wang D., et al. *Opt. Express*, **22** (18), 21739 (2014).
126. Kiktenko E.O., Pozhar N.O., Duplinskiy A.V., Kanapin A.A., Sokolov A.S., Vorobey S.S., Miller A.V., Ustimchik V.E., Anufriev M.N., Trushechkin A.T., Yunusov R.R., Kurochkin V.L., Kurochkin Yu.V., Fedorov A.K. *Quantum Electron*., **47** (9), 798 (2017) [*Kvantovaya Elektron*., **47** (9), 798 (2017)].
127. Praveenkumar S., Jaya T., Vijayan K., Yuvaraj S. *Microprocess. Microsyst.*, **82**, 103820 (2021).
128. Eraerds P., Legre M., Zhang J., Zbinden H., Gisin N. *J. Lightwave Technol*., **28** (6), 952 (2010).
129. Yu C., Shangguan M., Xia H., Zhang J., Dou X., Pan J.-W. *Opt. Express*, **25** (13), 14611 (2017).
130. Kirkwood R.A. *Superconducting single photon detectors for quantum information processing*. PhD Thesis (University of Glasgow, 2017).
131. Barbieri C., Naletto G., Occhipinti T., Facchinetti C., Verroi E., Giro E., Di Paola A., Billotta S., Zoccarato P., Bolli P., et al. *J. Mod. Opt*., **56** (2 – 3), 261 (2009).
132. Lee C., Johnson B., Jung T., Molnar A. *Sensors*, **16** (9), 1422 (2016).
133. Al-Rawhani M.A., Hu C., Giagkoulovits C., Annese V.F., Cheah B.C., Beeley J., Velugotla S., Accarino C., Grant J.P., Mitra S., et al. *IEEE Trans. Biomed. Eng*., **67** (2), 614 (2019).
134. Yin H.-L., Chen T.-Y., Yu Z.-W., Liu H., You L.-X., Zhou Y.-H., Chen S.-J., Mao Y., Huang M.-Q., Zhang W.-J., et al. *Phys. Rev. Lett*., **117** (19), 190501 (2016).
135. Chen J.-P., Zhang C., Liu Y., Jiang C., Zhang W., Hu X.-L., Guan J.Y., Yu Z.-W., Xu H., Lin J., et al. *Phys. Rev. Lett*., **124** (7), 070501 (2020).
136. Pugh C.J., Kaiser S., Bourgoin J.-P., Jin J., Sultana N., Agne S., Anisimova E., Makarov V., Choi E., Higgins B.L., et al. *Quantum Sci. Technol*., **2** (2), 024009 (2017).
137. Liao S.-K., Lin J., Ren J.-G., Liu W.-Y., Qiang J., Yin J., Li Y., Shen Q., Zhang L., Liang X.-F., et al. *Chin. Phys. Lett*., **34** (9), 090302 (2017).

138. Takenaka H., Carrasco-Casado A., Fujiwara M., Kitamura M., Sasaki M., Toyoshima M. *Nat. Photonics*, **11** (8), 502 (2017).
139. Yin J., Cao Y., Li Y.-H., Liao S.-K., Zhang L., Ren J.-G., Cai W.-Q., Liu W.-Y., Li B., Dai H., et al. *Science*, **356**, 1140 (2017).
140. Ren J.-G., Xu P., Yong H.-L., Zhang L., Liao S.-K., Yin J., Liu W.-Y., Cai W.-Q., Yang M., Li L., et al. *Nature*, **549**, 70 (2017).
141. Liao S.-K., Cai W.-Q., Handsteiner J., Liu B., Yin J., Zhang L., Rauch D., Fink M., Ren J.-G., Liu W.-Y., et al. *Phys. Rev. Lett*., **120** (3), 030501 (2018).